ARTICLE

Cytomatrix proteins CAST and ELKS regulate retinal photoreceptor development and maintenance

Akari Hagiwara[1] , Yosuke Kitahara[2]*, Chad Paul Grabner[4,5]* , Christian Vogl[4] , Manabu Abe[6], Ryo Kitta[1], Keisuke Ohta[3] , Keiichiro Nakamura[3] , Kenji Sakimura[6], Tobias Moser[4,5,7] , Akinori Nishi[2], and Toshihisa Ohtsuka[1]

At the presynaptic active zone (AZ), the related cytomatrix proteins CAST and ELKS organize the presynaptic release machinery. While CAST is known to regulate AZ size and neurotransmitter release, the role of ELKS and the integral system of CAST/ELKS together is poorly understood. Here, we show that CAST and ELKS have both redundant and unique roles in coordinating synaptic development, function, and maintenance of retinal photoreceptor ribbon synapses. A CAST/ELKS double knockout (dKO) mouse showed high levels of ectopic synapses and reduced responses to visual stimulation. Ectopic formation was not observed in ELKS conditional KO but progressively increased with age in CAST KO mice with higher rates in the dKO. Presynaptic calcium influx was strongly reduced in rod photoreceptors of CAST KO and dKO mice. Three-dimensional scanning EM reconstructions showed structural abnormalities in rod triads of CAST KO and dKO. Remarkably, AAV-mediated acute ELKS deletion after synapse maturation induced neurodegeneration and loss of ribbon synapses. These results suggest that CAST and ELKS work in concert to promote retinal synapse formation, transmission, and maintenance.

Introduction

The presynaptic active zone (AZ) is a highly specialized subcellular compartment, where neurotransmitter-containing synaptic vesicles dock within a few tens of nanometers from voltage-gated calcium channels (Ca_V) and are prepared to fuse with the plasma membrane in a Ca^{2+}-dependent manner. Synaptic signal transduction is coordinated by protein complexes at the pre- and post-synaptic sites. In this framework, the presynaptic release machinery is regulated by cytomatrix at the AZ (CAZ) proteins, including Munc13, RIM, Bassoon, CAST (also named ELKS2α or ERC2), and ELKS (ELKS1α or ERC1; Gundelfinger and Fejtova, 2012; Südhof, 2012; Ohtsuka, 2013) that compose the presynaptic density (Hagiwara et al., 2005). These proteins are believed to perform a variety of roles such as formation and maintenance of synapses, tethering and docking synaptic vesicles at AZ release sites, and recruitment of Ca_V channels to the AZ. In addition to studies investigating the functional properties of the individual CAZ proteins in various synapses (Südhof, 2012; Hamada and Ohtsuka, 2018), work using combinatorial deletion of proteins, such as ELKS (CAST/ELKS) and RIM, or RIM and RIM-BP, has shown a strong reduction of docked vesicles or presynaptic dense projections—classical morphological markers of the AZ (Acuna et al., 2016; Wang et al., 2016).

Elaborate electron-dense structures are found at invertebrate T-bar synapses and ribbon synapses of the vertebrate eye and ear (Zhai and Bellen, 2004; Wichmann and Moser, 2015; Maxeiner et al., 2016; Petzoldt et al., 2016). These so-called "synaptic ribbons" are mainly composed of RIBEYE and CAZ proteins, including Bassoon, Piccolo, RIM, and CAST (Schmitz et al., 2000; Dick et al., 2001; Khimich et al., 2005; Ohtsuka, 2013; Maxeiner et al., 2016; Jean et al., 2018). In this framework, genetic deletion of RIBEYE eliminated the ribbon and disrupted both fast and sustained neurotransmitter release from bipolar cells (BCs; Maxeiner et al., 2016). In contrast, in auditory hair cells, ribbon loss upon RIBEYE deletion led to elaborate developmental compensation that resulted in the formation of multiple ribbonless AZs at each synaptic contact with spiral ganglion neurons that sustained basic release rates (Becker et al., 2018; Jean et al., 2018). Bassoon, another multi-domain CAZ protein, exerts an essential role in anchoring the synaptic ribbon at the AZ membrane, and loss of Bassoon results in impaired transmission at retinal and cochlear synapses (Dick et al., 2003; Khimich et al., 2005; Buran et al., 2010). Deletion of RIM2 reduced Ca^{2+} influx and affected release from rod terminals without changing rod ribbon synapse anatomy (Grabner et al., 2015; Löhner et al., 2017). At hair cell

[1]Department of Biochemistry, Faculty of Medicine, University of Yamanashi, Yamanashi, Japan;   [2]Department of Pharmacology, Kurume University School of Medicine, Fukuoka, Japan;   [3]Department of Anatomy, Kurume University School of Medicine, Fukuoka, Japan;   [4]Institute for Auditory Neuroscience and Inner Ear Lab, University Medical Center Göttingen, Göttingen, Germany;   [5]Synaptic Nanophysiology Group, Max Planck Institute for Biophysical Chemistry, Göttingen, Germany;   [6]Department of Cellular Neurobiology, Brain Research Institute, Niigata University, Niigata, Japan;   [7]Collaborative Research Center 889, University of Göttingen, Göttingen, Germany.

*Y. Kitahara and C.P. Grabner contributed equally to this paper;   Correspondence to Tobias Moser: tmoser@gwdg.de;   Toshihisa Ohtsuka: tohtsuka@yamanashi.ac.jp.

synapses, RIM2 disruption reduced the number of presynaptic Ca^{2+} channels and tethered synaptic vesicles at the AZ membrane. Conversely, deletion of CAST, a molecular scaffold and protein interaction hub, reduced rod photoreceptor AZ size, ultimately leading to impaired electroretinogram (ERG) responses and attenuated contrast sensitivity (tom Dieck et al., 2012).

While the presynaptic function of CAST has been analyzed in various preparations over recent years (Takao-Rikitsu et al., 2004; Kaeser et al., 2009; tom Dieck et al., 2012; Held et al., 2016; Kobayashi et al., 2016), other work on invertebrate CAST/ELKS homologues in *Caenorhabditis elegans* (ELKS) and *Drosophila melanogaster* (bruchpilot) suggest additional roles in synapse formation and the promotion of AZ assembly, respectively (Dai et al., 2006; Kittel et al., 2006). In contrast, the role of presynaptic ELKS remains largely enigmatic, mainly owing to the fact that in vertebrates ELKS isoforms are ubiquitously expressed and constitutive ELKS knockout (KO) mice are embryonic-lethal (Deguchi-Tawarada et al., 2004; Liu et al., 2014). ELKS is characterized by higher solubility than CAST in spite of its 92% sequence similarity with the neuron-specific CAST (Ohtsuka et al., 2002; Fig. S1). Since ELKS is also found at retinal ribbon synapses (Deguchi-Tawarada et al., 2006), we hypothesized that ELKS may—at least partially—compensate for the loss of CAST from the synapse, thereby masking the individual contributions of CAST/ELKS family proteins in synaptic processes.

To elucidate the roles of ELKS and CAST in retinal photoreceptor AZ formation and maintenance as well as in synaptic processing of visual information, the present study established ELKS conditional KO (cKO) and CAST KO/ELKS cKO (double KO [dKO]) mice using a Crx-Cre line (Nishida et al., 2003) for retina-specific deletion of ELKS. Comprehensive functional and anatomical analysis revealed that CAST and ELKS have both redundant and unique roles at the rod photoreceptor ribbon synapse. Remarkably, the acute depletion of ELKS from the mature retinal network induced a concomitant loss of ribbon synapses and photoreceptors. Therefore, we conclude that organization of release machinery with CAST and ELKS plays functional and anatomical roles in photoreceptor neurotransmission, the disruption of which may cause progressive blindness due to synaptic and neural remodeling.

Results

Combined ablation of ELKS and CAST from retinal photoreceptors causes impaired visual responses

First, we generated an ELKS cKO crossing *ELKS^flox/flox* mice with Crx-Cre mice for targeted deletion of exon 11 in the retina (Fig. 1 A and Fig. S1; Nishida et al., 2003; Dong et al., 2018). Deletion of exon 11 causes a frame shift in exons 12 and 13, resulting in the premature termination of all ELKS isoforms including α, β, γ, δ, and ε (Fig. S1 C; Nakata et al., 2002), and hence elimination of all functional ELKS protein from the retina. ELKS cKO mice showed normal development, while mice carrying *CAST^-/-* and *ELKS^flox/flox* alleles as well as Crx-Cre (CAST/ELKS dKO) exhibited slightly smaller body weight and eye size (Fig. S2 A and Table S1). In accordance with a previous study (Deguchi-Tawarada et al., 2006), immunohistochemical analysis of ELKS expression in

the retina confirmed the presence of ELKS in the outer plexiform layer (OPL), where rod and cone terminals form synapses with BCs and horizontal cells (HCs). In contrast, in the OPL of ELKS cKO mice, only a small number of nonspecific speckles could be observed (Fig. 1 C). Similarly, the inner plexiform layer (IPL), containing the synapses formed by BC, amacrine, and ganglion cells, also showed ELKS immunofluorescence in control retinae that was absent in ELKS cKO mice (Fig. 1 C). Immunoblotting of synapse-related proteins from retinal lysates confirmed the targeted deletion of ELKS and CAST in the respective individual KOs and the removal of both proteins from the dKO (Fig. 1, D and E). As previously reported (tom Dieck et al., 2012), we found a threefold, potentially compensatory up-regulation of ELKS in the CAST KO mice. Conversely, CAST expression increased in ELKS cKO mice (Fig. 1, D and E; and Fig. S2, B–E), indicating mutual compensatory up-regulation of both proteins. Interestingly, expression of RIM1/2, which directly interacts with CAST/ELKS (Ohtsuka et al., 2002; Wang et al., 2002; Deguchi-Tawarada et al., 2004), was decreased in the ELKS cKO and dKO mice, but not in the CAST KO mice (Fig. 1, D and E). We speculate that the reduction in RIM1/2 protein levels reflects the loss of an ELKS-RIM interaction, because the observed reduction of RIM1/2 was comparable between ELKS cKO and dKO mice (Fig. 1 E) despite the prominent up-regulation of CAST in ELKS cKO mice.

To characterize visual function in mice of the different genotypes, we measured the ERG under scotopic conditions (Fig. 1, F–I). In these experiments, dark-adapted mice were exposed to dim light flashes of increasing intensity to trigger progressively stronger retinal responses. Here, the a-wave, indicating photoreceptor transduction, was unaltered across all genotypes. In contrast, the scotopic b-wave, reflecting rod photoreceptor transmission, was reduced in all mutants, from near normal in ELKS cKO to about half in the CAST KO mice, and nearly abolished in dKO. The oscillatory potentials, primarily reflecting the activity of the inner retina, were reduced in CAST KO and even further in dKO mice. Hence, the reduction in scotopic ERG signals indicates impaired synaptic transmission in the OPL and IPL in response to loss of CAST, a phenotype that is further aggravated by additional deletion of ELKS.

Loss of photoreceptor ribbon synapses and enhanced formation of ectopic ribbon synapses

Next, we analyzed the formation of retinal layers. The thickness and the density of nuclei layers (outer nuclear layer [ONL] and inner nuclear layer [INL]) were not significantly different across the genotypes in the adult retina (~10 wk old; Fig. S2, F and G). In contrast, both CAST KO and dKO showed a reduction in OPL thickness (Fig. S2, F and G). In addition, dKO led to significant reduction in IPL thickness (Fig. S2, F and G), while the thicknesses of OPL and IPL were normal in the ELKS cKO. The reduced thickness of the synaptic layers suggests extensive remodeling of retinal synapses without major cell loss in the absence of CAST and ELKS.

The distribution of presynaptic proteins (i.e., RIBEYE and vGluT1) and synaptic connectivity with BCs and HCs was assessed by immunohistochemistry using cell type–specific markers (protein kinase C and calbindin, respectively; Fig. 2, A and B).
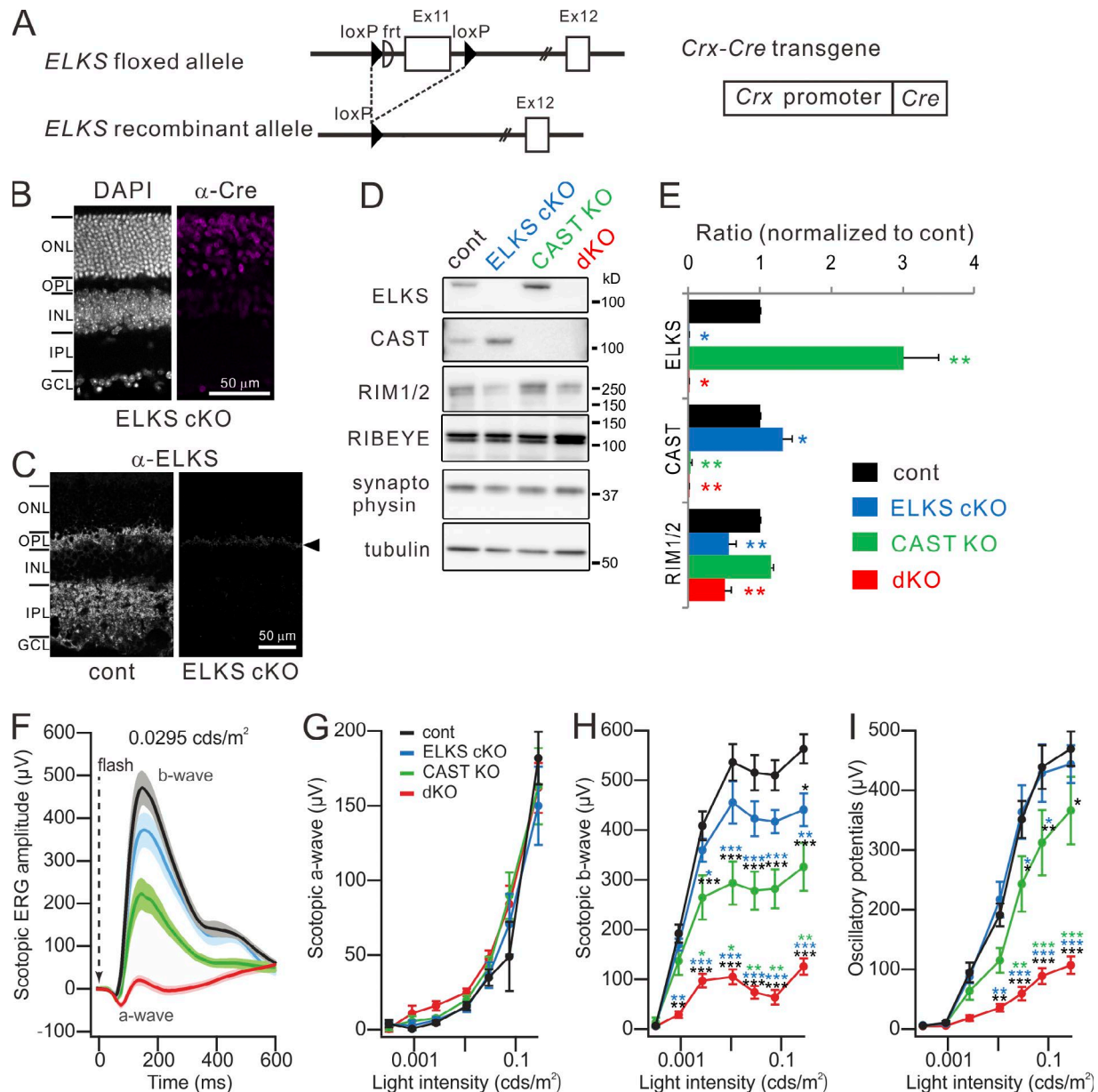
Figure 1. **Genetic ablation of CAST and ELKS in the retina elicits impaired photoreceptor neurotransmission. (A)** The *ELKS flox* allele contains two loxP sequences flanking exon 11 of mouse *ELKS*. Conditional ablation of *ELKS* was mediated by crossing ELKS flox mice with *Crx-Cre* mice. **(B and C)** Immunohistochemistry for Cre expression and subsequent depletion of ELKS from ELKS cKO retina. **(C)** ELKS distribution in both OPL and IPL is depleted, although a slight background signal is detected at the OPL (arrowhead). GCL, ganglion cell layer. Bars, 50 µm. **(D and E)** Western blotting of adult (9–12-wk-old) retinal homogenates of mutant mice with indicated antibodies. **(E)** ELKS expression ($n = 6$) is increased in the CAST KO and, conversely, CAST expression ($n = 4$) is enhanced in the ELKS cKO. RIM1/2 expression ($n = 3$) is reduced by ∼50% in ELKS cKO and dKO mice; mean ± SEM; asterisks indicate statistical comparison to control. *, $P < 0.05$; **, $P < 0.01$ (one-way ANOVA, post hoc Tukey test). **(F–I)** Scotopic ERG responses recorded from control ($n = 7$), ELKS cKO ($n = 6$), CAST KO ($n = 7$), and dKO ($n = 7$). Scotopic b-waves (H), indicating downstream BC activity, and oscillatory potentials (I) are significantly impaired in CAST KO, and even more dramatically in dKO, while a-waves (G), indicating phototransduction, remained unaffected. Colored asterisks indicate statistical comparison to the respectively colored genotypes and statistical significance. mean ± SEM; *, $P < 0.05$; **, $P < 0.01$; ***, $P < 0.001$ (two-way ANOVA, post hoc Tukey test).

Both CAST KO and dKO mice exhibited an increase in the formation of ectopic ribbon synapses in the ONL, which were accompanied by abnormal sprouting of BCs and HCs dendritic processes (Fig. 2, A and B). Here, we quantified ectopically formed synapses in the ONL by measuring the displacement of RIBEYE-positive spots from the OPL to the ONL (Fig. 2 C and Fig. S3, A and B). Immunolabeled ribbons were isolated from background noise by their fluorescent intensity and the spot size (see Materials and

methods). While ∼10% of synapses mislocalized to the ONL in the CAST KO, a staggering ∼40% of synapses formed ectopically in the dKO (Fig. 2 C). Similar to the ribbon marker, the presynaptic terminal marker vGluT1 also exhibited ectopic synapse formation in CAST KO and dKO mice (Fig. S3 C). Age-related synaptic remodeling was apparent from the increase in ectopic synapse probability with advancing age in the dKO: ectopic synapses were identified as early as 5 wk of age and further increased up to
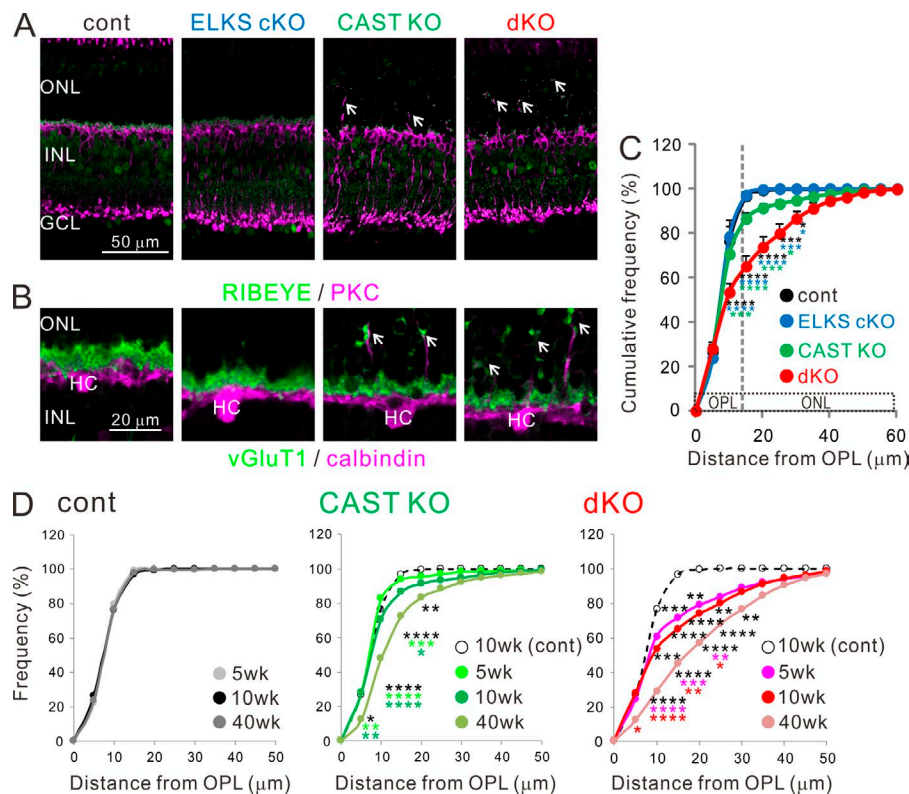
Hagiwara et al.
CAST/ELKS coordinate retinal ribbon synapse

Journal of Cell Biology 3995
https://doi.org/10.1083/jcb.201704076

Figure 2. **Increased occurrence of ectopic ribbon synapses in CAST KO and dKO retinae. (A and B)** Representative confocal images of immunolabeled retinal sections, showing distribution of presynaptic proteins (RIBEYE in A, vGluT1 in B; green) with respect to BCs (PKC; magenta; A) and HCs (calbindin; magenta; B). Ectopically localized synapses in the ONL of CAST KO and dKO retinae (indicated by white arrows). Bars, 50 μm in A; 20 μm in B. **(C)** Cumulative histogram of distance probability of RIBEYE puncta measured from the OPL. In adult (10-wk-old) control and ELKS cKO retinae, the frequency reaches ∼100% within 15–20 μm, indicating precise localization in the OPL. However, in the CAST KO and dKO, the frequency curve is right-shifted and 10–40% of ribbons are ectopically localized in the ONL; mean ± SEM; control (n = 4), ELKS cKO (n = 4), CAST KO (n = 6), and dKO (n = 7). **(D)** Cumulative histogram for distance probability of RIBEYE from 5–40-wk-old retinae. In the control retina, the distribution of synaptic ribbons is tightly packed in the OPL from young (5-wk-old) to aged (40-wk-old) retinas. In the CAST KO, where a few ectopic synapses were identified in 5- and 10-wk-old retinae, ectopic distribution at 40 wk is significantly increased. Furthermore, many ectopic synapses are detected even at 5 and 10 wk of age in dKO compared with the 10-wk-old control group. Ectopic synapses are further increased at 40 wk, indicating an age-dependent, progressive phenotype in CAST KO and dKO. Control, 5 wk (n = 3), 10 wk (n = 4), 40 wk (n = 4); CAST KO, 5 wk (n = 4), 10 wk (n = 6), 40 wk (n = 5); dKO, 5 wk (n = 4), 10 wk (n = 7), and 40 wk (n = 4). Colored asterisks indicate statistical significance from respective colored genotypes. *, P < 0.05; **, P < 0.01; ***, P < 0.001; ****, P < 0.0001 (two-way ANOVA followed by post hoc Bonferroni).

>40 wk (Fig. 2 D and Fig. S3 D). A similar observation was made in CAST KO mice, but to a lesser extent (Fig. 2 D and Fig. S3 D).

We also calculated the density of RIBEYE spots within the OPL and ONL (Fig. 3, A–C). The densities of such spots in ONL plus OPL were similar for control and ELKS cKO mice. However, in the CAST KO and dKO mice, the density of RIBEYE spots decreased by ∼30% (Fig. 3 A). Inspection of the ONL only showed a several-fold increase in density of RIBEYE spots in the dKO, while the CAST KO was less strongly affected (Fig. 3 B). Finally, the density of RIBEYE spots in the OPL of CAST KO and dKO mice was greatly reduced to ∼50% and 40% compared with controls, respectively (Fig. 3 C). Since RIBEYE spot detection was set to the size threshold, the resultant spot size was comparable between genotypes (control = 0.48 ± 0.045 μm², ELKS cKO = 0.53 ± 0.035, CAST KO = 0.45 ± 0.022, and dKO = 0.46 ± 0.018). However, a previous study (tom Dieck et al., 2012) reported that loss of CAST reduces rod ribbon size. Hence, due to threshold exclusion of smaller ribbons in the mutants, our current analysis of RIBEYE immunofluorescence spots did not reveal a reduction in ribbon size (see Roles of CAST and ELKS in the formation of rod triads and tom Dieck et al., 2012) and likely underestimated the density. Therefore, we also performed conventional EM to examine rod ribbon density in the OPL at higher resolution. The density of ribbon-bearing rod terminals in the OPL was drastically reduced in both CAST KO and dKO to a similar extent, while it was unchanged in the ELKS cKO (Fig. 3, D and E). Furthermore, we investigated the synaptic vesicle distribution at rod ribbon synapses taken from randomly selected ultrathin sections. The density of ribbon-associated synaptic vesicles was slightly decreased in dKO, but did not differ significantly from control or CAST KO (Fig. 3, F and G). The Pearson's correlation coefficients between ribbon length and vesicle number were ∼0.4 for all genotypes (control = 0.41, ELKS cKO = 0.40, CAST KO = 0.46, and dKO = 0.43), indicating a scaled reduction of vesicle tethering capacity with decreasing ribbon size. Moreover, we analyzed the densities of freely floating synaptic vesicles in the cytoplasm of randomly selected rod terminals that possessed compartments of triads including ribbon synapses, and found them to be comparable between all genotypes (control = 130.5 ± 6.7 /μm² [n = 5], ELKS cKO = 144.5 ± 8.9 [n = 6], CAST KO = 155.4 ± 6.2 [n = 5], and dKO = 153.9 ± 6.2 [n = 5]).

Roles of CAST and ELKS in the formation of rod triads

In a previous study, CAST was shown to promote AZ size, light responses, and contrast sensitivity (tom Dieck et al., 2012). The present study further assessed the roles of CAST and ELKS in photoreceptor synapse formation and maintenance by investigating the ultrastructure of rod terminals, which form so-called "triads" between photoreceptor ribbon synapses and BC and HC processes ("tips"), using focused ion beam milling combined with scanning EM (FIB-SEM; Kitahara et al., 2016). Three terminals in the OPL from three different animals of each mouse strain were randomly chosen for 3D reconstruction (Fig. 4, Fig. S4, and Tables S2 and S3). Rod terminals possessed single mitochondria, and volume of neither individual terminals nor mitochondria
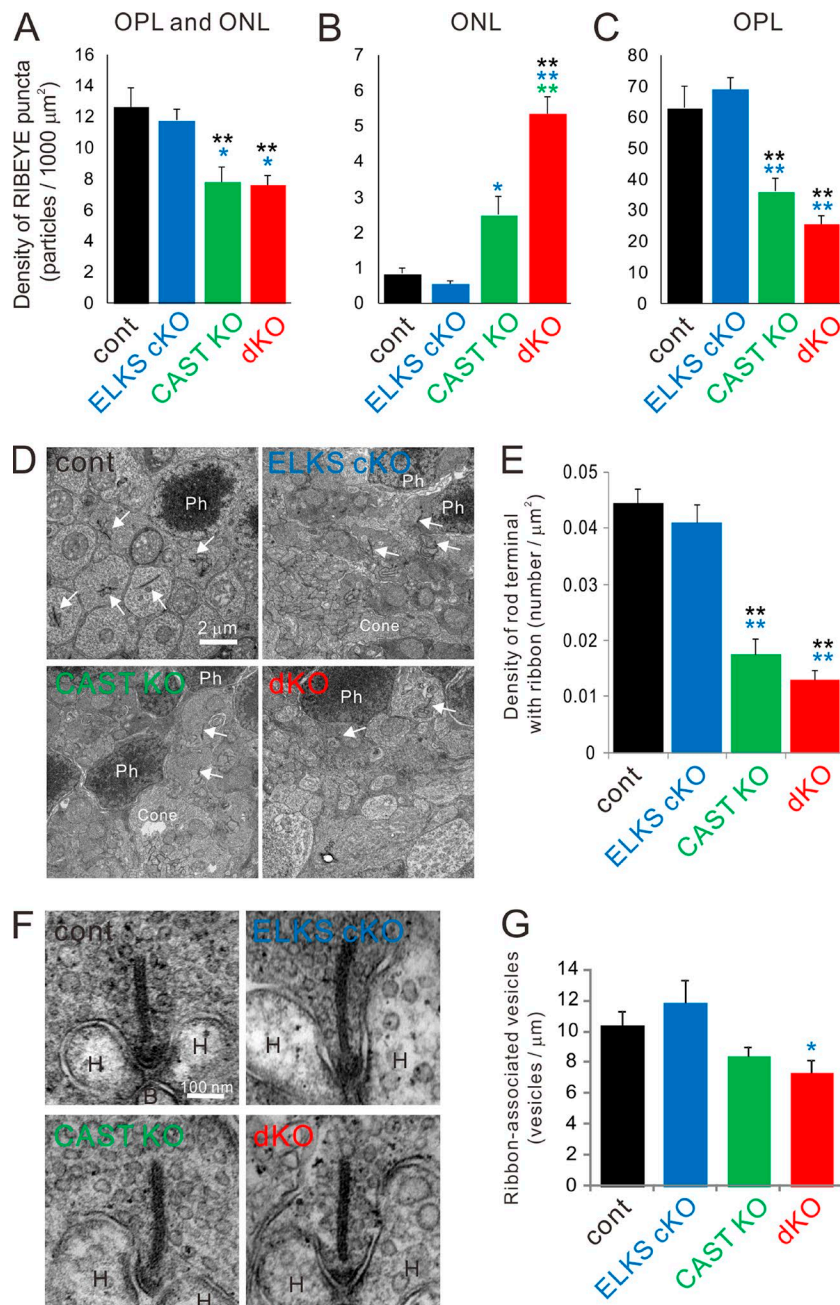
Hagiwara et al.
CAST/ELKS coordinate retinal ribbon synapse

Journal of Cell Biology
https://doi.org/10.1083/jcb.201704076

3996

Figure 3. **Genetic ablation of CAST/ELKS leads to fewer ribbon-bearing rod terminals in the ONL and attenuated vesicle distributions on presynaptic ribbons. (A–C)** Density of RIBEYE-labeled ribbon synapses in the entire area of OPL and ONL (A), ONL (B), and OPL (C). RIBEYE density in the entire area is significantly reduced in CAST KO and dKO. In detail, ectopic synapses in the ONL are significantly increased in CAST KO and dKO; dKO is further enhanced compared with CAST KO. Conversely, RIBEYE density in the OPL is reduced by almost half in CAST KO and dKO compared with the control and ELKS cKO. Colored asterisks indicate statistical significance from respective colored genotypes, mean ± SEM; control ($n = 4$), ELKS cKO ($n = 4$), CAST KO ($n = 6$), and dKO ($n = 7$). *, $P < 0.05$; **, $P < 0.01$ (one-way ANOVA followed by post hoc Tukey test). **(D and E)** Density of ribbon-bearing rod terminals was measured in electron micrographs taken at 2,500 magnification. Images from the ONL showed rod terminals with ribbons (arrows), cone terminals including several mitochondria and ribbons (Cone), and photoreceptor nucleus (Ph). The density of ribbon-bearing rod terminals was significantly decreased in CAST KO and dKO mice, mean ± SEM; control ($n = 24$), ELKS cKO ($n = 20$), CAST KO ($n = 22$), and dKO ($n = 24$). **, $P < 0.01$ (one-way ANOVA followed by post hoc Tukey test) **(F)** Representative images of rod terminals including ribbons (arrow) and horizontal (H) cell tips in 100,000 magnification images. **(G)** The number of ribbon-associated synaptic vesicles was significantly decreased in dKO compared with the ELKS cKO, mean ± SEM; control ($n = 5$), ELKS cKO ($n = 6$), CAST KO ($n = 5$), and dKO ($n = 5$). *, $P < 0.05$ (one-way ANOVA followed by post hoc Tukey test). Bars, 2 µm in D; 100 nm in F.

was significantly different between the genotypes (Tables S2 and S3). While we found BC tips to be comparable across all genotypes (Fig. 4 D and Fig. S4), the majority of HCs only exhibited a single tip in CAST KO and dKO mice. In contrast, control and ELKS cKO mice always possessed at least two tips (Fig. 4 E). Intriguingly, 3D reconstructions revealed that the single HC tip in the CAST KO and dKO mice branched before contacting the synaptic ribbon, forming a structure similar to that of the two HC tips that normally target the ribbon (Fig. 4 B and Fig. S4). Although the individual tip sizes (surface area and volume) remained unaltered across all genotypes (Tables S2 and S3 and Fig. S4), the loss of the second HC tip from the triad of CAST KO and dKO retinae led to a significant reduction of the accumulated surface area and volume of HC tips (Fig. 4 E, Fig. S4, and Tables S2 and S3). In CAST KO and dKO mice, overall HC counts, as measured by cal-

bindin staining, remained unaltered (Table S5). However, 3D reconstructions of HC branching from a tip within a triad revealed fewer branches with filopodia-like structures that were lacking tips (Fig. S4 E).

Photoreceptor ribbons have been proposed to play an important role in replenishing synaptic vesicles to the AZ (Jackman et al., 2009; Maxeiner et al., 2016). Hence, we next investigated synaptic ribbon morphology from 3D reconstructed images. In these experiments, reconstructed ribbons showed plate-like structures with a horseshoe-shaped appearance in the control and ELKS cKO (Fig. 4 C). However, compared with control, ribbon lengths were significantly decreased in all deletion mutants, with the highest and comparable severity in CAST KO and dKO (Fig. 4 G and Table S4). Moreover, we measured the shortest distance from the ribbon to the surface of BC tips, and found it to be
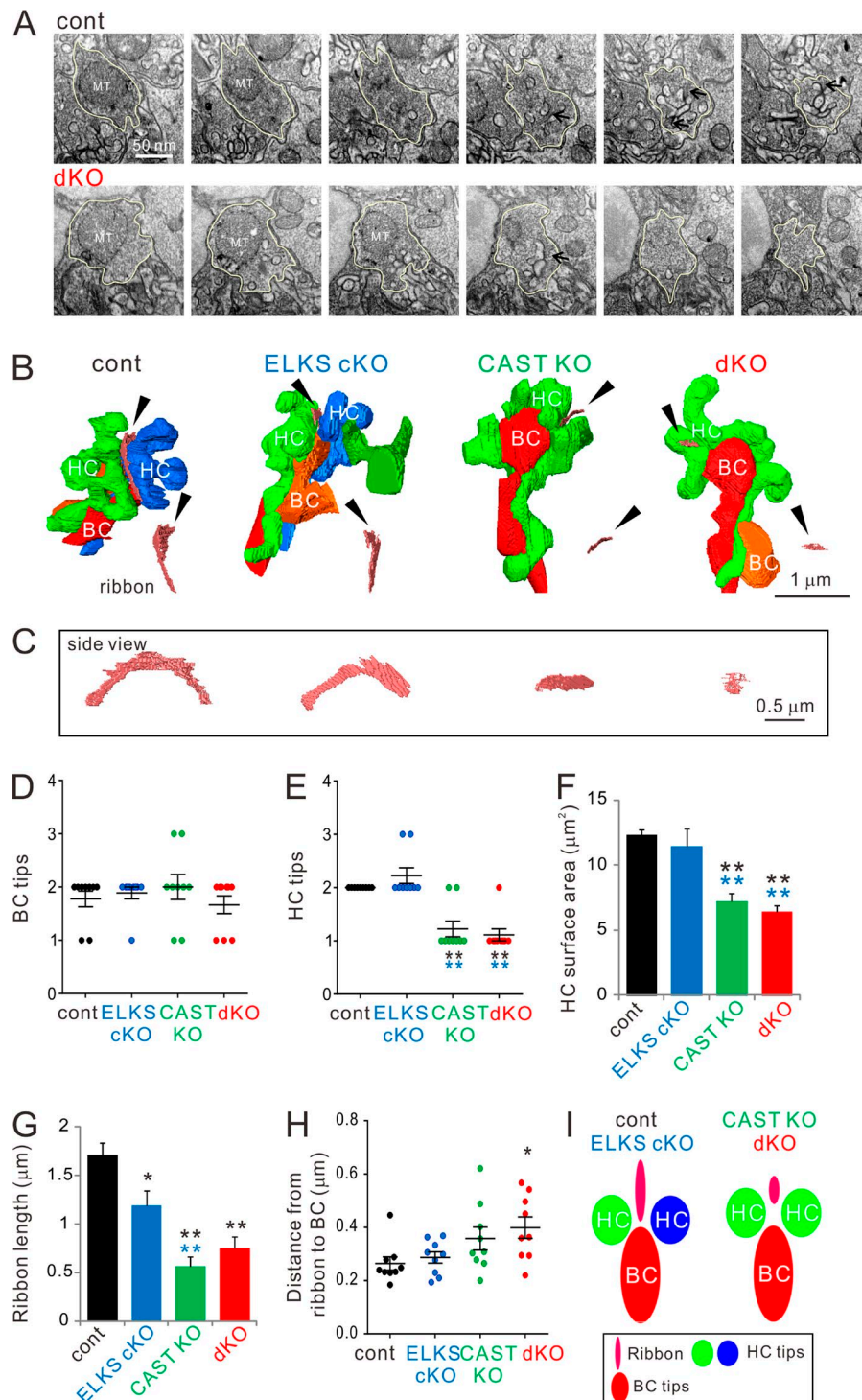
Figure 4. **3D reconstruction of rod terminals in the OPL shows morphological abnormalities in CAST KO and dKO retinae. (A)** Representative FIB-SEM images from control and dKO (300-nm interval). The rod terminals indicated by yellow lines were 3D-reconstructed in A. Arrows indicate synaptic ribbons. **(B and C)** Representative images of 3D-reconstructed triads were acquired by FIB-SEM. Small truncated ribbons (pink bands indicated by black arrowheads) occur in a single HC tip in the CAST KO and dKO. HC (green, blue), BC (red, orange). Representative examples of ribbons are illustrated (as viewed from the bottom; black arrowhead); ribbon profiles are demonstrated in C. **(D–F)** Analysis of BC and HC tips inserted into rod terminals. Consistent with the reduced HC tip numbers (E) in CAST KO and dKO retinae, the respective accumulated HC surface areas (F) are also significantly decreased. Colored asterisks indicate significant differences compared with the respective colored genotypes, mean ± SEM; $n = 9$. **, $P < 0.01$ (one-way ANOVA, post hoc Tukey test). **(G)** The entire ribbon length in each terminal was significantly decreased in all three deletion mutants compared with control. **(H)** The shortest distance from the ribbon to the BC tip is significantly increased in the dKO, mean ± SEM; $n = 9$. *, $P < 0.05$; **, $P < 0.01$ (one-way ANOVA, post hoc Tukey test). **(I)** Simplified schematic models of triad complexes composed by a ribbon, two HCs, and one or two BCs. In CAST KO and dKO retinae, the two HC tips switch to a branched single tip with reduced ribbon length.

significantly longer in the dKO compared with control (Fig. 4 H). The CAST KO fell in between, showing no statistical difference in ribbon–BC tip separation for the CAST KO versus dKO, nor the CAST KO versus control.

Overall, the 3D reconstructions of FIB-SEM data revealed impaired triad formation that can be summarized as follows for the CAST KO and dKO: (a) reduced HC branching, (b) decreased surface area of the HC processes in the rod triads, (c) diminution of ribbon size (and to a lesser extent in ELKS cKO), and (d) increased width of the synaptic cleft between rod ribbons and

BC tips. In other words, CAST and ELKS codetermine the structure of the rod ribbon synapses and synaptic connectivity with HCs and BCs (Fig. 4 I), with CAST exerting a more prominent role than ELKS. Combining these findings with conventional EM, the rod AZs of CAST KO and dKO mice are similar in many ways: both show truncated ribbons and comparable vesicle density. The increased distance from the ribbon to the BC tips might not suffice to explain the severely attenuated scotopic b-waves and the enhanced formation of ectopic synapses in the dKO. Although ELKS itself seems to contribute in a minor way to the presynaptic

morphology, it may affect AZ function. Therefore, we next probed rod Ca_V channels to assess if their function behaves differently in the CAST KO and dKO.

Roles of CAST and ELKS in the voltage-dependent calcium influx at rod terminals

L-type $Ca_V1.4$ channels localize to rod ribbon synapses (Liu et al., 2013; Zabouri and Haverkamp, 2013), and previous work suggests that its pore-forming α1 subunit (tom Dieck et al., 2012) and α2δ4 auxiliary subunit (Wang et al., 2017) traffic to the downsized ribbons formed by CAST KO rods. Therefore, we performed whole-cell voltage-clamp recordings from rods to test the behavior of the $Ca_V1.4$ channels in acute retinal slices from adult control, CAST KO, and dKO mice (4 mo of age). Calcium currents (I_{Ca}) were recorded from rod somata located on the ONL border to the OPL, where the synaptic ribbon is contained in the soma compartment (Fig. 5 A; Grabner et al., 2015). While the example control recording showed an inward I_{Ca} with a peak amplitude of approximately –9 pA when the voltage was ramped from –70 to +50 mV, the response acquired from a CAST KO was essentially flat (Fig. 5, B and C). To illustrate the excitability of cells without I_{Ca}, the cells were also given steps from –70 to –90 mV to activate the hyperpolarizing inward current (I_h) carried by hyperpolarizatoin-activated cyclic nucleotide-gated channels (Bader et al., 1982). The hyperpolarizing voltage step followed by a depolarizing voltage ramp activated an I_h current in rods (Fig. 5 D), but I_{Ca} was seldom detected in CAST KO and dKO (Fig. 5 E). In addition, rod somata located in the ONL (about a single row of soma away from the OPL) were also patched, thus allowing the visualization of the rod's short axon linked to the small terminal (Fig. S5 A). Again, the I_{Ca} was either strongly reduced or almost absent in CAST KO and dKO mice, while I_h currents as well as an outward current related to the inner segment (Barnes, 1994; Grabner et al., 2015) were routinely observed (Fig. S5, B and C). The summarized data show a drastically reduced I_{Ca} in CAST KO and dKO relative to control, while the KO mice were not significantly different from one another (Fig. 5 F and Fig. S5 G). In addition, we estimated the voltage where the I_{Ca} reaches half maximal amplitude on the voltage ramp ($V_{1/2}$) in recordings with measurable I_{Ca}, which can indicate modulation of Ca_V gating. The $V_{1/2}$ values were similar across the genotypes: control = –29 ± 1.5 mV (n = 9 cells), CAST KO = –30 ± 1.4 mV (n = 4 cells), and dKO = –31 ± 1.9 mV (n = 7 cells). However, it should be noted that only half of CAST KO (four of eight cells) and dKO (7 of 16 cells) had sufficient I_{Ca} amplitudes (>0.5 pA) to estimate the $V_{1/2}$. These results indicate that CAST plays an essential role in maintaining Ca^{2+} entry into rod terminals.

Acute deletion of ELKS induces photoreceptor remodeling and elimination of ribbon synapses

ELKS is ubiquitously expressed, including in nonneural tissues, and constitutive ELKS KO is embryonic-lethal (Deguchi-Tawarada et al., 2004; Liu et al., 2014). Therefore, developmental compensation by other presynaptic terminal proteins might mask the ELKS KO phenotype in our preparation. To address this issue, we next investigated ELKS function in photoreceptors after intact synapse
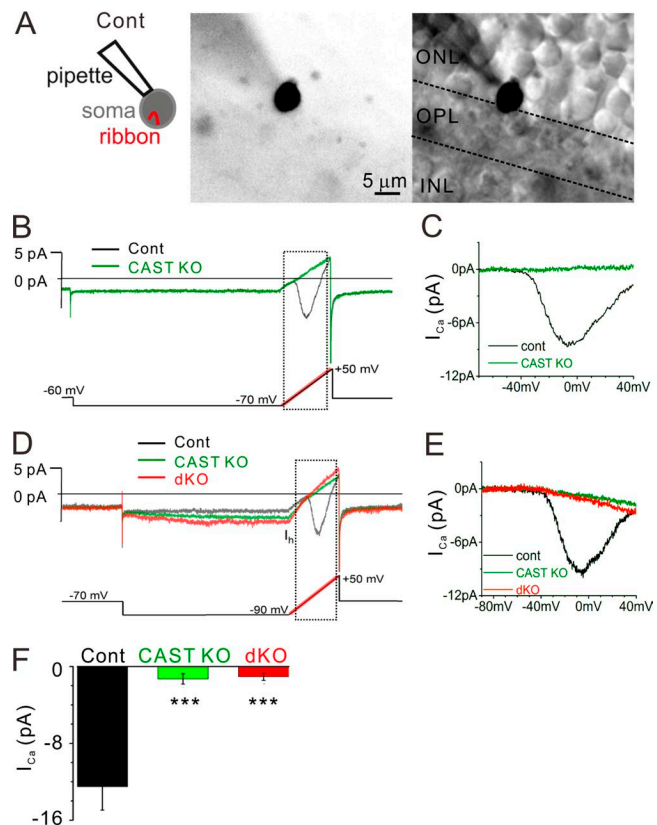

Figure 5. **I_{Ca} is drastically reduced in CAST KO and dKO rod photoreceptors. (A)** Representative images of a recording made from a soma located at the ONL–OPL border, where the ribbon is contained in the soma compartment. The cell is filled with an Alexa Fluor 488 via recording pipette. Bars, 5 µm. **(B and C)** Control rod current trace (black line) exhibits the current-voltage (I-V) behavior for rod voltage-dependent $Ca_V1.4$ channels (recording from the cell that is presented in A). The voltage protocol is indicated at the bottom, and the ramp portion is highlighted in red. The current response to the voltage ramp (indicated by dashed square) is leak subtracted and presented in C. In contrast to the control, the CAST KO trace (green line) lacks an inward current. **(D and E)** The voltage protocol further tests the excitability of the cells by stepping from –70 to –90 mV to activate a I_h. While all genotypes showed inward I_h, CAST KO and dKO mice exhibited no signs of I_{Ca}. Current traces are presented after 1 kHz low-pass filtering. **(F)** The average peak amplitudes including the ramps starting at –70 and –90 mV were drastically reduced in CAST KO and dKO mice. In contrast, there were no significant differences between CAST KO and dKO mice (P < 0.7), mean ± SEM. control, n = 9 cells from seven mice; CAST KO, n = 8 cells from seven mice; dKO, n = 16 cells from 11 mice; ***, P < 0.001 (two-sided Student's t test).

formation and maturation. In these experiments, acute ELKS depletion was achieved by intravitreal injection of adeno-associated virus serotype 5 (AAV5) encoding Cre (AAV5-CAGGS-nCre) into ~5-wk-old $ELKS^{fl/fl}$ animals. At 3 wk after injection, robust Cre recombinase expression was observed in photoreceptors (Cre-positive; Fig. 6 and Fig. S6). Acute ELKS cKO induced a reduction in ONL thickness, suggesting substantial photoreceptor loss (Fig. 6). Ribbon synapse density in the OPL (as assessed by RIBEYE immunolabeling) decreased by 64% in the Cre-positive region compared with the proximal Cre-negative regions (Fig. 6, B, D, and F). The acute depletion of ELKS in CAST KO retinae led to partial ablation of the ONL, as illustrated by an almost complete loss of ribbon synapses, i.e., 89% (Fig. 6 D and Fig. S5). Moreover, we have confirmed
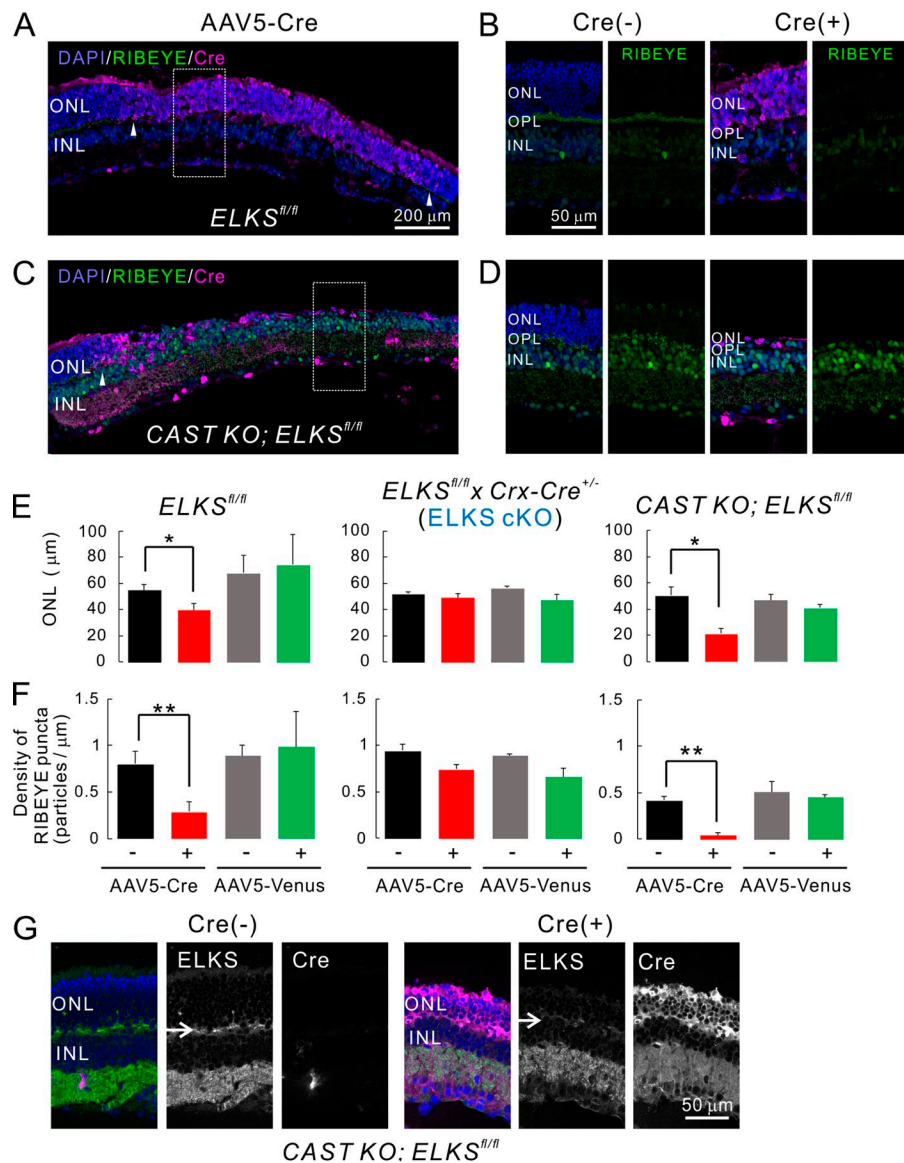
Hagiwara et al.
CAST/ELKS coordinate retinal ribbon synapse

Journal of Cell Biology 3999
https://doi.org/10.1083/jcb.201704076

Figure 6. **Acute, AAV-mediated, ELKS depletion in photoreceptors induces photoreceptor degeneration. (A–D)** Acute induction of ELKS cKO and dKO via AAV5-CAGGS-nCre. Subretinal injection of AAV5 produces mosaic Cre expression in the retina (Cre[+], indicated by arrowheads in A and C). (B and D) Immunolabeling of RIBEYE (green) in the OPL is reduced in the Cre-positive area (expansion of area indicated by white rectangle in A and C), when directly compared with adjacent Cre-negative regions (Cre[−] in B and D). Bars, 200 µm in A and C, 50 µm in B and D. **(E and F)** Quantitative analysis of ONL thickness and RIBEYE density. In *ELKS^{fl/fl}* and *CAST KO; ELKS^{fl/fl}* mice, ONL thickness (E) and RIBEYE density (F) are significantly decreased in Cre-positive regions, although Venus expression does not affect these parameters. Importantly, acute Cre expression in *ELKS^{fl/fl} x Crx-Cre^{+/−}* (ELKS cKO) mice affects neither ONL thickness nor RIBEYE density, indicating a CAST/ELKS-dependent mechanism as the underlying cause; mean ± SEM. ONL: *ELKS^{fl/fl}*; Cre (*n* = 5 mice), Venus (*n* = 2), *ELKS^{fl/fl} x Crx-Cre^{+/−}*; Cre (*n* = 3), Venus (*n* = 3), *CAST KO; ELKS^{fl/fl}*; Cre (*n* = 3), and Venus (*n* = 3). RIBEYE: *ELKS^{fl/fl}*; Cre (*n* = 5), Venus (*n* = 2), *ELKS^{fl/fl} x Crx-Cre^{+/−}*; Cre (*n* = 3), Venus (*n* = 2), *CAST KO; ELKS^{fl/fl}*; Cre (*n* = 4), and Venus (*n* = 3). *, P < 0.05; **, P < 0.01 (two-sided Student's *t* test). **(G)** Ablation of ELKS in the OPL in *CAST KO; ELKS^{fl/fl}* Cre (+) retina (arrows). Bar, 50 µm.

that acute ablation of ELKS by AAV-Cre expression caused loss of ELKS protein at the OPL in *ELKS^{fl/fl}* mice (Fig. 7 A), which difference was even more drastic in *CAST KO ELKS^{fl/fl}* mice (Fig. 6 G). Because ELKS expression was up-regulated in the CAST KO retina (Fig. 1 D), acute dKO after synapse formation might induce photoreceptor degeneration more severely than acute ELKS cKO. To establish whether these effects were indeed a direct result of ELKS elimination from photoreceptors and exclude adverse effects due to the virus application, we also injected AAV5-CAGGS-nCre into *ELKS^{fl/fl} x Crx-Cre^{+/−}* (ELKS cKO) mice. Importantly, acute Cre expression had no quantifiable effects on ELKS KO photoreceptors, ONL thickness, or RIBEYE density (Fig. 6, E and F; and Fig. S6 B). Consistent with these findings, injection of an AAV5 encoding the fluorescent transduction marker Venus showed no effect on ONL thickness or RIBEYE density (Fig. 6, E and F; and Fig. S6, C–E).

Finally, to further characterize photoreceptor degeneration, we performed TUNEL assays to detect apoptotic cells in retinal cryosections obtained from injected mice 2 wk after AAV5-Cre administration. Here, besides the TUNEL reagents, retinal serial cryosections were simultaneously subjected to anti-ELKS and anti-Cre antibodies. In contrast to the nontransduced control parts of these retinae, where we mostly detected TUNEL negative cells, clear TUNEL staining was observed in Cre expressing photoreceptors within the ONL, accompanied by a reduction of ELKS in the OPL (Fig. 7 A). In contrast, injection of AAV5-Cre into ELKS cKO did not generate a large proportion of TUNEL-positive cells in the ONL, as confirmed by the maintained ONL thickness (Fig. S6 F). Therefore, the reduction of the ONL in acute ELKS KO by AAV5-Cre injection into *ELKS^{fl/fl}* eyes was likely caused by photoreceptor apoptosis. The reduction in the thickness of the ONL induced by AAV5-Cre could be prevented by the coinjection of AAV5-CAST-IRES-Venus, but not with AAV5-Venus in the *CAST KO ELKS^{fl/fl}* retina (Fig. 7, B–E). In these experiments, the expression of the transduction marker Venus was substantially weaker in AAV5-CAST-IRES-Venus transduction. We speculate that this finding can be attributed to the construct design and less efficient translation of Venus due to the IRES motif. To clarify this point, we assessed the transduction efficiency of AAV-CAST-
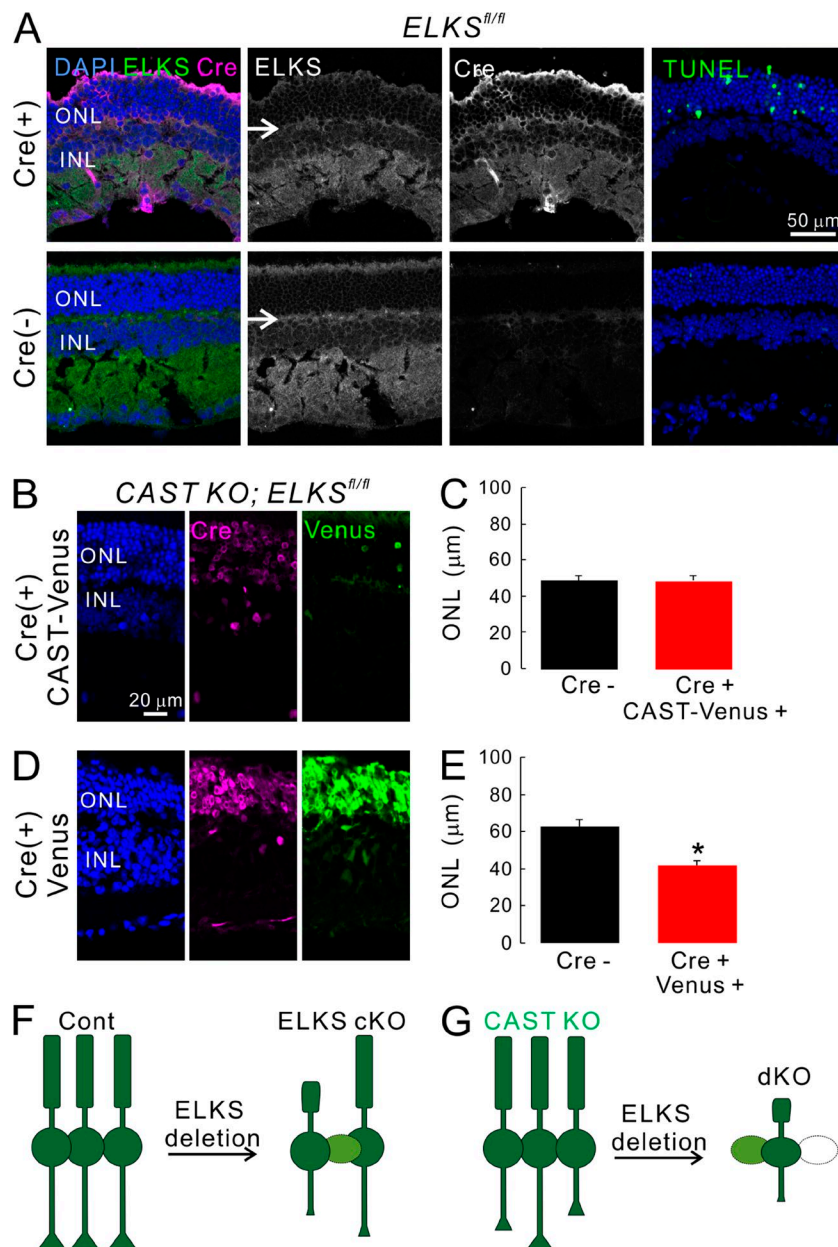
Figure 7. **Acute depletion of ELKS in retina induces apoptotic cell death in photoreceptors, which can be prevented by simultaneous expression of CAST. (A)** Acute induction of ELKS cKO by injection of AAV5-CAG GS-nCre in *ELKS*^{fl/fl} retina (Cre⁺) showed multiple TUNEL positive cells in the ONL, while no TUNEL-positive cells were observed in Cre negative retinae (Cre⁻). ELKS expression in the OPL was ablated in *ELKS*^{fl/fl} Cre⁺ retina (arrows). **(B–E)** Acute depletion of ELKS by AAV5-CAG GS-nCre in *CAST KO; ELKS*^{fl/fl} mice were effectively rescued by simultaneous injection of AAV5-CAGGS-CAST-IRES-Venus. The ONL thickness was not significantly decreased (C; Cre⁻ [$n = 18$], Cre⁺ CAST-Venus [$n = 19$]). In contrast, the simultaneous injection of AAV5-IRES-Venus failed to rescue the significant reduction of ONL thickness (E; Cre⁻ [$n = 10$], Cre⁺ Venus [$n = 16$]); mean ± SEM; *, $P < 0.05$ (two-sided Student's *t* test). Bars, 50 µm in A, 20 µm in B and D. **(F and G)** Simplified schematic model summarizing the findings from photoreceptors by ELKS ablation. Acute ELKS depletion after maturation of retinal network induces degeneration of photoreceptors (light green and white cells), which was further enhanced in the CAST KO retina.

IRES-Venus in cultured neurons, in which CAST was strongly expressed in Venus-positive neurons (Fig. S6, F and G).

The acute depletion of ELKS in retinae lacking CAST led to partial ablation of the ONL, as illustrated by an almost complete loss of ribbon synapses (Fig. 6, D and F). Hence, acute ablation of ELKS after synapse formation might induce photoreceptor degeneration more severely in the absence of CAST, indicating overlapping roles between ELKS and CAST, as suspected from the observed compensatory up-regulation of ELKS expression in CAST KO retinae (Fig. 1 D and Fig. 6 G).

Discussion

Photoreceptors transform light into membrane voltages, which in turn drives signal transmission to the inner retina. The molecular physiology of synaptic transmission at rod photorecep-

tors remains incompletely understood. In the current study, we analyzed structural and functional changes in the retina upon deletion of the highly homologous multi-domain proteins of the AZ, CAST, and ELKS. This study revealed that both CAST KO and CAST/ELKS dKO rod terminals exhibited altered triad ribbons and HC processes, drastically reduced calcium influx and comparable loss of synaptic ribbons from the OPL, and, finally, exhibited extensive synaptic remodeling involving ectopic synapses in the ONL. In addition, rod ribbon synapses of the dKO exhibited fewer ribbon-associated synaptic vesicles and a greater separation of the ribbon from the BC dendrite. Moreover, dKO mice exhibited the largest number of ectopic ribbon synapses in the ONL. Taken together, these additional deficits are likely to account for the stronger reduction in the scotopic ERG b-wave in dKO mice, compared with that observed in the CAST KO mice. In contrast to CAST, ablation of ELKS early in development did not

significantly alter ERG responses or ribbon anatomy. However, ELKS deletion after synapse formation caused massive loss of ribbon synapses and photoreceptors, which was partially halted by CAST. In summary, our data indicate that CAST and ELKS are critical for visual processing by exhibiting both redundant and complementary functions in synapse formation, function and maintenance in retinal rod photoreceptors.

A role for CAST/ELKS in presynaptic Ca²⁺ influx

Using whole-cell voltage-clamp recording from rod photoreceptors (Grabner et al., 2015; Wang et al., 2017), which gives unprecedented access to a synaptic ribbon, we demonstrated that CAST elimination greatly reduces the Ca^{2+} influx via Ca_V channels. This finding is consistent with previous studies in which CAST deletion not only decreases ribbon lateral expansion but also reduces presynaptic $Ca_V1.4$ abundance at rod AZ (tom Dieck et al., 2012; Wang et al., 2017). Interestingly, RIM2, which interacts with CAST (Wang et al., 2002) and is located at rod ribbons near $Ca_V1.4$ channels, also promotes Ca^{2+} influx into mouse rods (Grabner et al., 2015). A role of CAST/ELKS in regulating presynaptic Ca^{2+} influx has also been reported in cultured hippocampal neurons. One previous study reported that action potential–driven changes in Ca^{2+} levels at the nerve terminals were lower than in control mice despite apparently normal expression of Ca_V channels (Liu et al., 2014). In accord with this finding, another study reported a direct interaction of CAST with Ca_V α1 and β subunits, and further reported a CAST-dependent hyperpolarizing shift in the voltage dependence of presynaptic Ca^{2+} channels upon coexpression in a heterologous expression system (Kiyonaka et al., 2012). Loss of CAST from rods greatly reduced the magnitude of Ca^{2+} currents. Taken together, these results suggest that CAST directly or indirectly regulates Ca_V abundance and function.

Morphological abnormalities of rod synapses in CAST KO and dKO mice

The impact of the loss of CAST/ELKS on the molecular architecture of rod triads was investigated by 3D reconstruction from a set of serial images using FIB-SEM (Kitahara et al., 2016). In these experiments, we observed varying degrees of ribbon size reduction in all deletion mutants (Fig. 4), consistent with a previously proposed scaffolding role of CAST/ELKS that facilitates the lateral expansion and structural integrity of retinal ribbons (tom Dieck et al., 2012). Interestingly, neither the limited reduction of ribbon size (<30%) nor the observed lateral fragmentation of ribbon bodies (Table S4) significantly affected photoreceptor neurotransmission or ERG performance in ELKS cKO mice (Fig. 1, F–I). In contrast, the major reduction in ribbon length of ~50–70% in CAST KO and dKO mice severely impaired synaptic function and visual processing.

According to the 3D reconstruction of the rod terminal, a single HC tip triad was formed in the CAST KO and dKO mice (Fig. 4). Further 3D reconstruction of the HC tips revealed fewer branches and the occurrence of filopodia-like structures (Fig. S4 E). We assumed an HC morphological impairment caused by the absence of CAST in HCs, mostly because Crx-driven Cre recombinase could eliminate ELKS only in non-HC neurons in the INL (Fig. S4, F–H). Therefore, the phenotypes seen in HCs could

be explained by the cell-type–independent depletion of CAST in CAST KO and dKO mice. In this context, CAST localization at the growth cone was previously suggested to play a role in maturation of neural circuits in primary cultured neurons (Ohtsuka et al., 2002). Previous reports also showed comparable single HC tip morphology in deletion mutants of PlexinA4 and netrin-G ligand 2, which are selectively localized to HC neurites and tips, respectively (Matsuoka et al., 2012; Soto et al., 2013; D'Orazi et al., 2014).

Enhanced ectopic synapse formation in retinae of CAST/ELKS deletion mutants

We previously found that retinae of CAST KO exhibited ectopic ribbons (tom Dieck et al., 2012). In the current study, we found that the compound deletion of ELKS and CAST further confounded synapse stability. Several previous studies have shown that mutation or deletion of various proteins involved in synaptic transmission was associated with ectopic ribbon formation (Dick et al., 2003; Schmitz et al., 2006; Specht et al., 2007; Maxeiner et al., 2016). As an extreme example, depletion of synaptic vesicle protein cystein string protein α causes ectopic synapse formation in concert with massive photoreceptor degeneration (Schmitz et al., 2006). Bassoon is a prominent example of an AZ protein, which is essential for anchoring the photoreceptor ribbon to the AZ, and its deletion is associated with ectopic synapses (Dick et al., 2003). Moreover, mouse models of congenital stationary night blindness that carry mutations in the Ca^{2+} channels and/or its binding proteins are in accord with hypothesized causal relationship between loss of AZ structural as well as functional integrity and ectopic synapse formation (Haeseleer et al., 2004; Chang et al., 2006; Liu et al., 2013; Regus-Leidig et al., 2014). Thus, current data from CAST KO and dKO mice confirmed that impairment of neurotransmission drove ectopic synapse formation in the ONL, which was exacerbated with aging in CAST KO and dKO mice.

Synaptopathies and retinal degenerative disease

The remodeling of photoreceptors is a hallmark of various acquired retinal diseases, such as retinitis pigmentosa (RP), which is mostly classified as inherited retinal dystrophy. The progression of RP is variable, although continued photoreceptor degeneration ultimately leads to functional blindness (Kalloniatis et al., 2015). Although several gene mutations have been identified from severe RP forms (Ferrari et al., 2011), and gene therapeutic approaches are currently under development (Zarbin, 2016), the precise molecular mechanisms of RP progression are not well understood. Recent advances in stem cell therapy hold great promise for the treatment of advanced RP by transplantation of embryonic and induced pluripotent stem cells (Shirai et al., 2016; Zarbin, 2016). Nevertheless, it is of utmost importance to suppress disease progression and retain normal vision for as long as possible. Thus, it is important to (a) understand the factors that initiate and facilitate neural remodeling and (b) identify molecular targets that are amenable to genetic therapy. In the current study, we found that the loss of ELKS in mature ribbon synapses induces photoreceptor degeneration, which was not apparent in the Cre-mediated ELKS cKO model, suggesting a novel molecular mechanism that specifically induces photoreceptor remodeling

and degeneration (Fig. 7, G and H). Thus, to develop novel therapies for late-onset retinal neurodegenerative disease, future studies should (a) identify potential relationships between RP mutant genes and AZ proteins and (b) analyze functional roles of RP mutant genes in neurotransmitter release.

Materials and methods

Generation of ELKS cKO mice
The use of the animals was approved by the Institutional Committee for the Care and Use of Experimental Animals at the University of Yamanashi, Yamanashi, Japan.

Inducible retina-specific ELKS mutant mice were obtained by crossing *ELKS^flox/flox* mice (Dong et al., 2018) with *Crx-Cre* mice carrying Cre recombinase under control of the *Crx* promoter, which is an otx-like homeobox gene expressed abundantly in the retina (provided by T. Furukawa, Osaka University, Osaka, Japan; Nishida et al., 2003). The *ELKS^flox/flox* mice were further crossed with *CAST^-/-* (tom Dieck et al., 2012) to generate *CAST^-/-; ELKS^flox/flox* mice. The mice derived from crossing *ELKS^flox/flox* with *ELKS^flox/flox; Crx-Cre^+/-* mice and *CAST^-/-; ELKS^flox/flox* with *CAST^-/-; ELKS^flox/flox; Crx-Cre^+/-* mice were used for subsequent studies. Genotyping of ELKS cKO, CAST KO, and dKO mice by PCR was performed using the following primers: ELKS flox: ELKS flox forward, 5'-AAGGCCCAAACAGAAGTTGA-3', ELKS flox reverse, 5'-ATGATTTGCTTTCCCATGCT-3'; CAST WT/KO: CAST WT forward, 5'-GTCACCACGTCTGCCAAGGT-3', CAST KO forward, 5'-GACATAGCGTTGGCTACCCGT-3', CAST reverse, 5'-GGG CTTGAAGATCCAACATCG-3'; and Crx-Cre: LCB836-Cre1, 5'-GTC GATGCAACGAGTGATGA-3', LCB836-Cre2, 5'-AGCATTGCTGTC ACTTGGTC-3', mLC3ex3GT-Cre3, 5'-TGAGCGAGCTCATCAAGA TAATCAGGT-3', and mLC3ex3GT-Cre4, 5'-GTTAGCATTGAGCTG CAAGCGCCGTCT-3'.

Immunoblotting
Retina homogenates from the adult mutant mice were analyzed using Western blotting, and the signal intensity was quantified using ImageJ software (National Institutes of Health) from more than three independent experiments. The primary antibodies used for Western blotting were anti-ELKS (1:500, rabbit; Deguchi-Tawarada et al., 2004), anti-CAST (1:1,000, guinea pig; Ohtsuka et al., 2002), anti-RIM1/2 (1:1,000, rabbit; provided by S. Kiyonaka, Kyoto University, Kyoto, Japan; Kiyonaka et al., 2007; although it was originally described as RIM1, the antigen was designed from the consensus region of RIM1/2), anti-RIBEYE (1:1,000, rabbit; 192003; SYSY), anti-synaptophysin (1:2,000, mouse; AB5258; Chemicon), anti-GAPDH (1:5,000, HRP conjugate; 3683; Cell Signaling), and anti-tubulin (1:500, mouse; CP06; Oncogene).

Immunohistochemistry and image analysis
Under deep pentobarbital anesthesia, mice were transcardially fixed with 4% paraformaldehyde and 10% picric acid in 0.1 M phosphate buffer (pH 7.4). The retinae were dissected and cryoprotected in 30% (wt/vol) sucrose in PBS for >2 h. Pieces of retinae were mounted in OCT compound (Tissue-Tek) and sectioned at a thickness of 10 μm on a cryostat (HM525 NX; Thermo Fisher Scientific). The collected sections were blocked for 1 h in blocking solution (2% normal goat or horse serum, 10% block ace [Dainippon Pharmaceutical], and 0.2% Triton X-100 in PBS) and incubated in primary antibodies in blocking solution overnight at room temperature. The following primary antibodies were used: anti-RIBEYE (1:1,000, rabbit), anti-PKC (1:1,000, mouse; ab31; Abcam), anti-vGluT1 (1:1,000, guinea pig), anti-calbindin (1:2,000, mouse; C9848; Sigma-Aldrich), and anti-Cre (1:800, mouse; MAB3120; and 1:500, rabbit; 69050-3; Millipore). A guinea pig antiserum against vGluT1 was raised against mouse vGluT1 C-terminal 531–560 aa (NM020309; Miyazaki et al., 2003). The sections were further processed with appropriate Alexa Fluor–conjugated secondary antibodies for 1 h at room temperature. Immunolabeled samples were viewed using a confocal laser microscope (FV1200; Olympus) at room temperature.

Distribution of ribbon synapses
RIBEYE-immunolabeled images were obtained with oil-immersion 60× objective (NA 1.35) with 2× digital zoom, and then binary-transformed (threshold ~1,300) images were analyzed using the ImageJ particle analysis program (particles smaller than 20 pixels were eliminated; Fig. S3). The total number of particles in OPL and ONL were divided by the area to calculate the RIBEYE density. The distance of each particle from the bottom of OPL (y axis) was evaluated by generating histograms and plotted as the cumulative frequency (%) for display. The statistical significance of density and probability for each distance from ONL was analyzed using one-way ANOVA or two-way ANOVA, respectively.

Imaging with FIB-SEM and 3D reconstruction
The mice were transcardially perfused with 2% glutaraldehyde and 2% paraformaldehyde in 0.1 M phosphate buffer (pH 7.4). Retinal sections (thickness, 400 μm) were further en bloc stained with a reduced OTO staining method: 1.5% potassium ferrocyanide, 2% OsO$_4$, 1% thiocarbohydrazide7, and then 2% OsO$_4$. For counterstaining, sections were further treated with 4% uranyl acetate and Walton's lead aspartate solution. After staining, samples were dehydrated and embedded in epoxy resin (EPON812; TAAB). Specimens were subjected to FIB-SEM tomography (Quanta 3D FEG; FEI) as previously described (Kitahara et al., 2016). In brief, the embedded slices were placed on a metal stub and further trimmed with glass and diamond knives in an ultramicrotome (Ultracut E microtome; Leica). The slices were coated with an electroconductive layer of carbon, which prevented any charge. The metal stub with the slices was set on the FIB-SEM stage, and then serial section images were automatically obtained from the OPL of the retina. Serial images of the block face were acquired by repeated cycles of sample surface milling and imaging using the Slice & View G2 operating software (FEI). The milling was performed with a gallium ion beam at 30 kV with a current of 1.0 nA. The milling pitch was set to 15 nm/step. The images were acquired at an accelerating voltage of 2.5 kV. The other acquisition parameters were as follows: dwell time = 6 s/pixel and pixel size = 7.3 nm/pixel. The serial section images were reconstructed to 3D images and analyzed using Amira 5.5 software (FEI).

ERG recordings

Mice were adapted to the dark overnight and anesthetized by intraperitoneal injection of ketamine (0.125 mg/g) and xylazine (2.5 µg/g), and one pupil was dilated with 1% atropine sulfate. All preparations were done under a dim red light. A ring-like AgCl wire electrode, moistened by methylcellulose and NaCl solutions, was placed on the cornea, and a needle reference electrode was subcutaneously inserted above the nose with a ground electrode near the tail. A custom-designed Ganzfield illuminated by 25 white LEDs was used to produce light flashes of incremental luminances (0.0003 to 0.278 candela/m^2; measured by Mavolux, IPL 10530). Scotopic responses were recorded for a stimulus duration of 0.1 ms with an inter-stimulus interval of 5 s. Recorded potentials were amplified, filtered (<400 Hz for a-waves, <20 Hz for b-waves, and 30–400 Hz for oscillatory potentials), and sampled at a rate of 24 kHz. 10 responses were averaged per light intensity. For analysis, a-wave amplitudes were measured relative to the baseline, whereas b-wave amplitudes were estimated relative to the trough of the a-wave. All data were analyzed using custom-written MATLAB-based analysis routines. Statistical significance was assessed by repeated measures two-way ANOVA followed by post hoc Tukey corrected for multiple comparisons.

EM

For conventional EM, mice were perfused transcardially with 2% paraformaldehyde and 2% glutaraldehyde in 0.1 M phosphate buffer (pH 7.4). Retinal sections (thickness, 400 µm) were further post-fixed with 2% osmium tetroxide in phosphate buffer for 2 h, stained with 2–4% uranyl acetate for 1 h, and then embedded in Durcupan ACM (Fluka). Ultra-thin sections (thickness, 70 nm) were prepared with an ultramicrotome (Ultracut EM UC7; Leica) and counterstained with uranyl acetate and lead citrate. For analysis, images were captured at OPL with an electron microscope (H-7500; Hitachi). Density of ribbon bearing rod terminal was analyzed from EM images of 2,500 magnification (single image size: 125 µm^2) in which cone terminals containing several mitochondria and ribbons could be identified by chance. The probability of finding the cone terminal was almost 10% of the control rod terminal, which was not significantly different between genotypes. Synaptic vesicle distribution was analyzed at higher magnification (e.g., 100,000, 2.25 µm^2), and quantitative parameters were measured using ImageJ software.

AAV5-mediated Cre expression and image analysis

For AAV-mediated Cre, Venus, or CAST-Venus expression in the retina, plasmid encoding pAAV5-CAGGS-nCre, pAAV5-CAGGS-IRES-Venus, and pAAV5-CAGGS-CAST-IRES-Venus were prepared to generate the recombinant AAV5. To inject the virus into eyes, mice were anaesthetized at ∼5 wk of age with ketamine/xylazine by intraperitoneal injection. A 30-gauge needle was used to make a small hole in the temporal eye, below the cornea, and ∼1 µl of AAV virus was injected into the vitreous humor over the retina using a glass pipette. For rescue experiments, a mixture of pAAV5-CAGGS-nCre with pAAV5-CAGGS-CAST-IRES-Venus or pAAV5-CAGGS-IRES-Venus was injected.

Because Cre or Venus expression in photoreceptor neurons with AAV5 was "patchy" in the injected retinae, we took at least three Cre or Venus expression images (Cre[+], Venus[+]) and non-Cre or -Venus expression images (Cre[−], Venus [−]) from the same retina. For ONL thickness, the images were obtained using a 40× objective lens (NA 0.95). RIBEYE density was calculated from images taken with a 60× objective and a 2× digital zoom. ONL thickness and RIBEYE densities were analyzed using ImageJ and compared between Cre-positive and -negative regions using the Student's t test.

TUNEL assay

For the assessment of apoptosis, the DeadEnd Fluorometric TUNEL system (Promega) was applied to 10-µm-thick PFA-fixed retinal cryosections according to the manufacturer's instructions. To identify the Cre expression area in the retina, another serial cryostat section was PFA fixed and then immunolabeled with anti-ELKS (1:100) and anti-Cre (1:800) antibodies.

Whole-cell voltage clamp recording

Mice between 14 and 18 wk of age were tested. Preparation of retinal slices and whole-cell voltage clamp recordings were conducted as described previously (Grabner et al., 2015). Briefly, retinal slices (∼200 µm thickness) were prepared in the following mouse extracellular solution, which had a low Ca^{2+} concentration (in mM): 135 NaCl, 2.5 KCl, 0.5 CaCl$_2$, 1 MgCl$_2$, 10 glucose, and 15 Hepes, pH 7.35, with osmolality adjusted to 295 mOsm. Slices in the recording chamber were then continually perfused in mouse extracellular solution with 2.5 mM Ca^{2+} at a temperature of 30°C to 32°C. The intracellular solution contained the following reagents (in mM): 105 CsCH$_3$SO$_4$, 20 TEA-Cl, 2 MgCl$_2$, 5 MgATP, 0.2 NaGTP, 10 Hepes, 10 EGTA, and 10 µg/ml Alexa Fluor 488, with pH adjusted to 7.30 with CsOH to an osmolality of 285 to 290 mOsm. The theoretical junction potential generated with these intra- and extracellular solutions is estimated to be −12 mV. The voltage-clamp data are not presented with the −12 mV added (V$_{1/2}$ and current traces plotted over voltage are raw values). The hyperpolarizing I$_h$ current was monitored to confirm the intactness of the recording.

The ramp protocols were preceded by steps from −60 to −70 mV or −70 to −90 mV (to activate I$_h$), and then ramped to +50 mV at a speed of 1 V/s. Since these two ramp types gave very similar I$_{Ca}$ and V$_{1/2}$ values within cells, data were summarized by averaging together the different voltage ramps. Average values from five control cells for ramps starting at −70 and −90 mV were as follows: I$_{Ca}$, 12.1 vs 11.8 pA (P = 0.95), and V$_{1/2}$, −28 vs −30 mV (P = 0.61).

Statistical analysis

Data are presented as mean ± SEM. Data distribution was assumed to be normal, but this was not formally tested. Statistical significance was analyzed using one-way ANOVA, two-way ANOVA, or two-sided Student's t test as indicated in each figure legend and in Table S6.

Online supplemental material

Fig. S1 shows the details of ELKS cKO with amino acid sequence of CAST and ELKS and their different solubility. Fig. S2 and Table S1 show the characterization of each genotype of mice including

Hagiwara et al.
CAST/ELKS coordinate retinal ribbon synapse

Journal of Cell Biology
https://doi.org/10.1083/jcb.201704076

4004

body weight and eyeball size, original data of immunoblotting, and retinal layer formation. Fig. S3 shows the analysis of ectopic ribbon synapse immunolabeled with RIBEYE and vGluT1. Fig. S4 and Tables S2, S3, and S4 give the additional data from the 3D-reconstructed rod terminal from each genotype of mice. Fig. S4 demonstrates lower expression of Cre recombinase in HC and Table S5 shows the line density of HC was not significantly different between genotypes. Fig. S5 shows the recoding of Ca^{2+} current from rod photoreceptors with inner segments. Though the traces of Ca^{2+} current with inner segments showed outward current, the peak amplitude and $V_{1/2}$ were not significantly different from the soma without inner segments. Then the data were pooled and statistically analyzed between genotypes. Fig. S6 shows the AAV-mediated Cre and Venus expression in *ELKS*^{fl/fl}, ELKS cKO (*ELKS*^{fl/fl} *x Crx-Cre*^{+/−}), and *CAST KO; ELKS*^{fl/fl} mice. Fig. S6, G and H, also showed the AAV-mediated expression of CAST and Venus in primary culture neurons for rescue experiments. Table S6 shows summary of statistical analysis.

Acknowledgments

References

Acuna, C., X. Liu, and T.C. Südhof. 2016. How to make an active zone: Unexpected universal functional redundancy between RIMs and RIM-BPs. *Neuron.* 91:792–807. https://doi.org/10.1016/j.neuron.2016.07.042

Bader, C.R., D. Bertrand, and E.A. Schwartz. 1982. Voltage-activated and calcium-activated currents studied in solitary rod inner segments from the salamander retina. *J. Physiol.* 331:253–284. https://doi.org/10.1113/jphysiol.1982.sp014372

Barnes, S. 1994. After transduction: response shaping and control of transmission by ion channels of the photoreceptor inner segments. *Neuroscience.* 58:447–459. https://doi.org/10.1016/0306-4522(94)90072-8

Becker, L., M.E. Schnee, M. Niwa, W. Sun, S. Maxeiner, S. Talaei, B. Kachar, M.A. Rutherford, and A.J. Ricci. 2018. The presynaptic ribbon maintains vesicle populations at the hair cell afferent fiber synapse. *eLife.* 7:e30241. https://doi.org/10.7554/eLife.30241

Buran, B.N., N. Strenzke, A. Neef, E.D. Gundelfinger, T. Moser, and M.C. Liberman. 2010. Onset coding is degraded in auditory nerve fibers from mutant mice lacking synaptic ribbons. *J. Neurosci.* 30:7587–7597. https://doi.org/10.1523/JNEUROSCI.0389-10.2010

Chang, B., J.R. Heckenlively, P.R. Bayley, N.C. Brecha, M.T. Davisson, N.L. Hawes, A.A. Hirano, R.E. Hurd, A. Ikeda, B.A. Johnson, et al. 2006. The *nob2* mouse, a null mutation in *Cacna1f*: anatomical and functional abnormalities in the outer retina and their consequences on ganglion cell visual responses. *Vis. Neurosci.* 23:11–24. https://doi.org/10.1017/S095252380623102X

D'Orazi, F.D., S.C. Suzuki, and R.O. Wong. 2014. Neuronal remodeling in retinal circuit assembly, disassembly, and reassembly. *Trends Neurosci.* 37:594–603. https://doi.org/10.1016/j.tins.2014.07.009

Dai, Y., H. Taru, S.L. Deken, B. Grill, B. Ackley, M.L. Nonet, and Y. Jin. 2006. SYD-2 Liprin-α organizes presynaptic active zone formation through ELKS. *Nat. Neurosci.* 9:1479–1487.

Deguchi-Tawarada, M., E. Inoue, E. Takao-Rikitsu, M. Inoue, T. Ohtsuka, and Y. Takai. 2004. CAST2: identification and characterization of a protein structurally related to the presynaptic cytomatrix protein CAST. *Genes Cells.* 9:15–23.

Deguchi-Tawarada, M., E. Inoue, E. Takao-Rikitsu, M. Inoue, I. Kitajima, T. Ohtsuka, and Y. Takai. 2006. Active zone protein CAST is a component of conventional and ribbon synapses in mouse retina. *J. Comp. Neurol.* 495:480–496. https://doi.org/10.1002/cne.20893

Dick, O., I. Hack, W.D. Altrock, C.C. Garner, E.D. Gundelfinger, and J.H. Brandstätter. 2001. Localization of the presynaptic cytomatrix protein Piccolo at ribbon and conventional synapses in the rat retina: comparison with Bassoon. *J. Comp. Neurol.* 439:224–234. https://doi.org/10.1002/cne.1344

Dick, O., S. tom Dieck, W.D. Altrock, J. Ammermüller, R. Weiler, C.C. Garner, E.D. Gundelfinger, and J.H. Brandstätter. 2003. The presynaptic active zone protein bassoon is essential for photoreceptor ribbon synapse formation in the retina. *Neuron.* 37:775–786. https://doi.org/10.1016/S0896-6273(03)00086-2

Dong, W., T. Radulovic, R.O. Goral, C. Thomas, M. Suarez Montesinos, D. Guerrero-Given, A. Hagiwara, T. Putzke, Y. Hida, M. Abe, et al. 2018. CAST/ELKS proteins control voltage-gated Ca^{2+} channel density and synaptic release probability at a mammalian central synapse. *Cell Reports.* 24:284–293.e6. https://doi.org/10.1016/j.celrep.2018.06.024

Ferrari, S., E. Di Iorio, V. Barbaro, D. Ponzin, F.S. Sorrentino, and F. Parmeggiani. 2011. Retinitis pigmentosa: genes and disease mechanisms. *Curr. Genomics.* 12:238–249. https://doi.org/10.2174/138920211795860107

Grabner, C.P., M.A. Gandini, R. Rehak, Y. Le, G.W. Zamponi, and F. Schmitz. 2015. RIM1/2-mediated facilitation of Cav1.4 channel opening is required for Ca^{2+}-stimulated release in mouse rod photoreceptors. *J. Neurosci.* 35:13133–13147. https://doi.org/10.1523/JNEUROSCI.0658-15.2015

Gundelfinger, E.D., and A. Fejtova. 2012. Molecular organization and plasticity of the cytomatrix at the active zone. *Curr. Opin. Neurobiol.* 22:423–430. https://doi.org/10.1016/j.conb.2011.10.005

Haeseleer, F., Y. Imanishi, T. Maeda, D.E. Possin, A. Maeda, A. Lee, F. Rieke, and K. Palczewski. 2004. Essential role of Ca^{2+}-binding protein 4, a Cav1.4 channel regulator, in photoreceptor synaptic function. *Nat. Neurosci.* 7:1079–1087. https://doi.org/10.1038/nn1320

Hagiwara, A., Y. Fukazawa, M. Deguchi-Tawarada, T. Ohtsuka, and R. Shigemoto. 2005. Differential distribution of release-related proteins in the hippocampal CA3 area as revealed by freeze-fracture replica labeling. *J. Comp. Neurol.* 489:195–216. https://doi.org/10.1002/cne.20633

Hamada, S., and T. Ohtsuka. 2018. CAST: Its molecular structure and phosphorylation-dependent regulation of presynaptic plasticity. *Neurosci. Res.* 127:25–32. https://doi.org/10.1016/j.neures.2017.12.005

Held, R.G., C. Liu, and P.S. Kaeser. 2016. ELKS controls the pool of readily releasable vesicles at excitatory synapses through its N-terminal coiled-coil domains. *eLife.* 5:e14862. https://doi.org/10.7554/eLife.14862

Jackman, S.L., S.Y. Choi, W.B. Thoreson, K. Rabl, T.M. Bartoletti, and R.H. Kramer. 2009. Role of the synaptic ribbon in transmitting the cone light response. *Nat. Neurosci.* 12:303–310. https://doi.org/10.1038/nn.2267

Jean, P., D. Lopez de la Morena, S. Michanski, L.M. Jaime Tobón, R. Chakrabarti, M.M. Picher, J. Neef, S. Jung, M. Gültas, S. Maxeiner, et al. 2018. The synaptic ribbon is critical for sound encoding at high rates and with temporal precision. *eLife.* 7:e29275. https://doi.org/10.7554/eLife.29275

Kaeser, P.S., L. Deng, A.E. Chávez, X. Liu, P.E. Castillo, and T.C. Südhof. 2009. ELKS2α/CAST deletion selectively increases neurotransmitter release at inhibitory synapses. *Neuron.* 64:227–239. https://doi.org/10.1016/j.neuron.2009.09.019

Kalloniatis, M., L. Nivison-Smith, J. Chua, M.L. Acosta, and E.L. Fletcher. 2015. Using the *rd1* mouse to understand functional and anatomical retinal remodeling and treatment implications in retinitis pigmentosa: A review. *Exp. Eye Res.* 150:1–16. https://doi.org/10.1016/j.exer.2015.10.019

Khimich, D., R. Nouvian, R. Pujol, S. Tom Dieck, A. Egner, E.D. Gundelfinger, and T. Moser. 2005. Hair cell synaptic ribbons are essential for synchronous auditory signalling. *Nature.* 434:889–894. https://doi.org/10.1038/nature03418

Kitahara, Y., K. Ohta, H. Hasuo, T. Shuto, M. Kuroiwa, N. Sotogaku, A. Togo, K. Nakamura, and A. Nishi. 2016. Chronic fluoxetine induces the enlargement of perforant path–granule cell synapses in the mouse dentate gyrus. *PLoS One.* 11:e0147307. https://doi.org/10.1371/journal.pone.0147307

Kittel, R.J., C. Wichmann, T.M. Rasse, W. Fouquet, M. Schmidt, A. Schmid, D.A. Wagh, C. Pawlu, R.R. Kellner, K.I. Willig, et al. 2006. Bruchpilot promotes active zone assembly, Ca2+ channel clustering, and vesicle release. *Science.* 312:1051–1054.

Kiyonaka, S., M. Wakamori, T. Miki, Y. Uriu, M. Nonaka, H. Bito, A.M. Beedle, E. Mori, Y. Hara, M. De Waard, et al. 2007. RIM1 confers sustained activity and neurotransmitter vesicle anchoring to presynaptic Ca2+ channels. *Nat. Neurosci.* 10:691–701.

Kiyonaka, S., H. Nakajima, Y. Takada, Y. Hida, T. Yoshioka, A. Hagiwara, I. Kitajima, Y. Mori, and T. Ohtsuka. 2012. Physical and functional interaction of the active zone protein CAST/ERC2 and the β-subunit of the voltage-dependent Ca^{2+} channel. *J. Biochem.* 152:149–159. https://doi.org/10.1093/jb/mvs054

Kobayashi, S., Y. Hida, H. Ishizaki, E. Inoue, M. Tanaka-Okamoto, M. Yamasaki, T. Miyazaki, M. Fukaya, I. Kitajima, Y. Takai, et al. 2016. The active zone protein CAST regulates synaptic vesicle recycling and quantal size in the mouse hippocampus. *Eur. J. Neurosci.* 44:2272–2284. https://doi.org/10.1111/ejn.13331

Liu, C., L.S. Bickford, R.G. Held, H. Nyitrai, T.C. Südhof, and P.S. Kaeser. 2014. The active zone protein family ELKS supports Ca^{2+} influx at nerve terminals of inhibitory hippocampal neurons. *J. Neurosci.* 34:12289–12303. https://doi.org/10.1523/JNEUROSCI.0999-14.2014

Liu, X., V. Kerov, F. Haeseleer, A. Majumder, N. Artemyev, S.A. Baker, and A. Lee. 2013. Dysregulation of Ca$_{(v)}$1.4 channels disrupts the maturation of photoreceptor synaptic ribbons in congenital stationary night blindness type 2. *Channels (Austin).* 7:514–523. https://doi.org/10.4161/chan.26376

Löhner, M., N. Babai, T. Müller, K. Gierke, J. Atorf, A. Joachimsthaler, A. Peukert, H. Martens, A. Feigenspan, J. Kremers, et al. 2017. Analysis of RIM expression and function at mouse photoreceptor ribbon synapses. *J. Neurosci.* 37:7848–7863. https://doi.org/10.1523/JNEUROSCI.2795-16.2017

Matsuoka, R.L., Z. Jiang, I.S. Samuels, K.T. Nguyen-Ba-Charvet, L.O. Sun, N.S. Peachey, A. Chédotal, K.W. Yau, and A.L. Kolodkin. 2012. Guidance-cue control of horizontal cell morphology, lamination, and synapse formation in the mammalian outer retina. *J. Neurosci.* 32:6859–6868. https://doi.org/10.1523/JNEUROSCI.0267-12.2012

Maxeiner, S., F. Luo, A. Tan, F. Schmitz, and T.C. Südhof. 2016. How to make a synaptic ribbon: RIBEYE deletion abolishes ribbons in retinal synapses and disrupts neurotransmitter release. *EMBO J.* 35:1098–1114. https://doi.org/10.15252/embj.201592701

Miyazaki, T., M. Fukaya, H. Shimizu, and M. Watanabe. 2003. Subtype switching of vesicular glutamate transporters at parallel fibre–Purkinje cell synapses in developing mouse cerebellum. *Eur. J. Neurosci.* 17:2563–2572. https://doi.org/10.1046/j.1460-9568.2003.02698.x

Nakata, T., T. Yokota, M. Emi, and S. Minami. 2002. Differential expression of multiple isoforms of the ELKS mRNAs involved in a papillary thyroid carcinoma. *Genes Chromosomes Cancer.* 35:30–37. https://doi.org/10.1002/gcc.10095

Nishida, A., A. Furukawa, C. Koike, Y. Tano, S. Aizawa, I. Matsuo, and T. Furukawa. 2003. *Otx2* homeobox gene controls retinal photoreceptor cell fate and pineal gland development. *Nat. Neurosci.* 6:1255–1263. https://doi.org/10.1038/nn1155

Ohtsuka, T. 2013. CAST: functional scaffold for the integrity of the presynaptic active zone. *Neurosci. Res.* 76:10–15. https://doi.org/10.1016/j.neures.2013.03.003

Ohtsuka, T., E. Takao-Rikitsu, E. Inoue, M. Inoue, M. Takeuchi, K. Matsubara, M. Deguchi-Tawarada, K. Satoh, K. Morimoto, H. Nakanishi, and Y. Takai. 2002. Cast: a novel protein of the cytomatrix at the active zone of synapses that forms a ternary complex with RIM1 and munc13-1. *J. Cell Biol.* 158:577–590. https://doi.org/10.1083/jcb.200202083

Petzoldt, A.G., J. Lützkendorf, and S.J. Sigrist. 2016. Mechanisms controlling assembly and plasticity of presynaptic active zone scaffolds. *Curr. Opin. Neurobiol.* 39:69–76. https://doi.org/10.1016/j.conb.2016.04.009

Regus-Leidig, H., J. Atorf, A. Feigenspan, J. Kremers, M.A. Maw, and J.H. Brandstätter. 2014. Photoreceptor degeneration in two mouse models for congenital stationary night blindness type 2. *PLoS One.* 9:e86769. https://doi.org/10.1371/journal.pone.0086769

Schmitz, F., A. Königstorfer, and T.C. Südhof. 2000. RIBEYE, a component of synaptic ribbons: a protein's journey through evolution provides insight into synaptic ribbon function. *Neuron.* 28:857–872. https://doi.org/10.1016/S0896-6273(00)00159-8

Schmitz, F., L. Tabares, D. Khimich, N. Strenzke, P. de la Villa-Polo, M. Castellano-Muñoz, A. Bulankina, T. Moser, R. Fernández-Chacón, and T.C. Südhof. 2006. CSPalpha-deficiency causes massive and rapid photoreceptor degeneration. *Proc. Natl. Acad. Sci. USA.* 103:2926–2931. https://doi.org/10.1073/pnas.0510060103

Shirai, H., M. Mandai, K. Matsushita, A. Kuwahara, S. Yonemura, T. Nakano, J. Assawachananont, T. Kimura, K. Saito, H. Terasaki, et al. 2016. Transplantation of human embryonic stem cell-derived retinal tissue in two primate models of retinal degeneration. *Proc. Natl. Acad. Sci. USA.* 113:E81–E90. https://doi.org/10.1073/pnas.1512590113

Soto, F., K.L. Watkins, R.E. Johnson, F. Schottler, and D. Kerschensteiner. 2013. NGL-2 regulates pathway-specific neurite growth and lamination, synapse formation, and signal transmission in the retina. *J. Neurosci.* 33:11949–11959. https://doi.org/10.1523/JNEUROSCI.1521-13.2013

Specht, D., S. Tom Dieck, J. Ammermüller, H. Regus-Leidig, E.D. Gundelfinger, and J.H. Brandstätter. 2007. Structural and functional remodeling in the retina of a mouse with a photoreceptor synaptopathy: plasticity in the rod and degeneration in the cone system. *Eur. J. Neurosci.* 26:2506–2515. https://doi.org/10.1111/j.1460-9568.2007.05886.x

Südhof, T.C. 2012. The presynaptic active zone. *Neuron.* 75:11–25. https://doi.org/10.1016/j.neuron.2012.06.012

Takao-Rikitsu, E., S. Mochida, E. Inoue, M. Deguchi-Tawarada, M. Inoue, T. Ohtsuka, and Y. Takai. 2004. Physical and functional interaction of the active zone proteins, CAST, RIM1, and Bassoon, in neurotransmitter release. *J. Cell Biol.* 164:301–311. https://doi.org/10.1083/jcb.200307101

tom Dieck, S., D. Specht, N. Strenzke, Y. Hida, V. Krishnamoorthy, K.-F.F. Schmidt, E. Inoue, H. Ishizaki, M. Tanaka-Okamoto, J. Miyoshi, et al. 2012. Deletion of the presynaptic scaffold CAST reduces active zone size in rod photoreceptors and impairs visual processing. *J. Neurosci.* 32:12192–12203. https://doi.org/10.1523/JNEUROSCI.0752-12.2012

Wang, S.S.H., R.G. Held, M.Y. Wong, C. Liu, A. Karakhanyan, and P.S. Kaeser. 2016. Fusion competent synaptic vesicles persist upon active zone disruption and loss of vesicle docking. *Neuron.* 91:777–791. https://doi.org/10.1016/j.neuron.2016.07.005

Wang, Y., X. Liu, T. Biederer, and T.C. Südhof. 2002. A family of RIM-binding proteins regulated by alternative splicing: Implications for the genesis of synaptic active zones. *Proc. Natl. Acad. Sci. USA.* 99:14464–14469.

Wang, Y., K.E. Fehlhaber, I. Sarria, Y. Cao, N.T. Ingram, D. Guerrero-Given, B. Throesch, K. Baldwin, N. Kamasawa, T. Ohtsuka, et al. 2017. The auxiliary calcium channel subunit α2δ4 is required for axonal elaboration, synaptic transmission, and wiring of rod photoreceptors. *Neuron.* 93:1359–1374.e6. https://doi.org/10.1016/j.neuron.2017.02.021

Wichmann, C., and T. Moser. 2015. Relating structure and function of inner hair cell ribbon synapses. *Cell Tissue Res.* 361:95–114. https://doi.org/10.1007/s00441-014-2102-7

Zabouri, N., and S. Haverkamp. 2013. Calcium channel-dependent molecular maturation of photoreceptor synapses. *PLoS One.* 8:e63853. https://doi.org/10.1371/journal.pone.0063853

Zarbin, M. 2016. Cell-based therapy for degenerative retinal disease. *Trends Mol. Med.* 22:115–134. https://doi.org/10.1016/j.molmed.2015.12.007

Zhai, R.G., and H.J. Bellen. 2004. The architecture of the active zone in the presynaptic nerve terminal. *Physiology (Bethesda).* 19:262–270.